Acta Materialia 299 (2025) 121434

Contents lists available at ScienceDirect

Acta Materialia

journal homepage: www.elsevier.com/locate/actamat

Full length article

Enhanced oxygen evolution on NiOOH through Fe-promoted transformation of β to γ phase

Da Chen [a], Daniele Perilli [a], Richard Dronskowski [b], Annabella Selloni [c], Cristiana Di Valentin [a,*]

[a] Materials Science Department, University of Milano-Bicocca, via R. Cozzi 55, I-20125 Milano, Italy
[b] Chair of Solid-State and Quantum Chemistry, Institute of Inorganic Chemistry, RWTH Aachen University, D-52056 Aachen, Germany
[c] Department of Chemistry, Princeton University, Princeton 08544 NJ, United States

ARTICLE INFO

Keywords:
OER
NiOOH
Fe-doping
Active phase
Hybrid density functional

ABSTRACT

It is widely agreed that Fe doping boosts the oxygen evolution reaction (OER) on NiOOH, but the mechanism and the active phase responsible for this enhancement are still under debate. Here we systematically investigate the atomic structure, electronic properties and OER activity of NiOOH using a hybrid density functional theory (DFT) method augmented with dispersion corrections. Our approach is validated by the good agreement between calculated properties and experiments. Chemical-bonding and phase transition energy analyses indicate that Fe doping weakens the adjacent O-H bonds and promotes the transformation from β-NiOOH to γ-NiOOH. The computed overpotentials of 0.68 V for β-NiOOH and 0.45 V for Fe-doped γ-NiOOH agree well with experiments. Our work reveals that the phase transition from β- to γ-NiOOH induced by Fe doping is the key factor to the enhanced OER activity of Fe-doped NiOOH relative to undoped NiOOH, which finally elucidates the long-standing debate on the OER mechanism and active phase of this material.

1. Introduction

Nickel oxides and oxyhydroxides (NiO_x) have attracted a great deal of attention due to their unique layered structure and electrochemical properties. According to the Bode diagram, NiO_x can be electrochemically cycled between its four phases, β-$Ni(OH)_2$, β-NiOOH, γ-NiOOH, and α-$Ni(OH)_2$ [1,2]. All of them are composed of NiO_2 layers, with all or part of the oxygens bonded to hydrogen atoms in the interlayer space. β-$Ni(OH)_2$ and β-NiOOH are ordered structures with small interlayer spacings, and β-NiOOH is the oxidation product of β-$Ni(OH)_2$ during charging [3,4]. With further overcharging β-NiOOH transforms into the less stable γ-NiOOH phase and at the same time the Ni oxidation state increases from 2.7–3.0 to 3.3–3.7 [5]. γ-NiOOH can subsequently be reduced to α-$Ni(OH)_2$ by discharging. Both γ-NiOOH and α-$Ni(OH)_2$ have large interlayer spacing, with m*ultiple species*, such as H_2O, OH^- and other ions, intercalated between the NiO_2 layers [6–8]. The structures of β-$Ni(OH)_2$ and β-NiOOH are relatively well-understood and assigned to the space group $P\bar{3}m1$ [9–11]. The oxygen atoms of β-$Ni(OH)_2$ are all saturated with protons, as shown in Figure S1. In contrast, only half of the oxygen atoms in β-NiOOH are bonded to H, due to partial deprotonation. The H positions cannot be experimentally determined due to their weak X-ray scattering cross-section.

Theoretical studies have proposed several favorable candidate structures for β-NiOOH, such as the phases dubbed as U, S, L and M in Ref. [12] (Figure S2). As for the electronic structure, experiments have shown that both β-$Ni(OH)_2$ and β-NiOOH are semiconductors with band gaps of 4.0 and 1.7–1.8 eV, respectively [13]. A higher value of 3.75 eV was also reported for the band gap of β-NiOOH [14], but this was probably due to sample contamination by NiO [15], which is characterized by a large band gap of 4.0 eV [16]. Indeed, a similar band gap of 3.6 eV has been reported for a mixture of NiO, $Ni(OH)_2$ and NiOOH [16]. Theoretically, previous studies using the PBE+U method (with $U = 5.5$ eV for Ni) reported a band gap of 3.0 eV for β-$Ni(OH)_2$ and incorrect metallic properties for some of the possible structures of β-NiOOH [9,15,17–19]. For β-NiOOH, He et al. reported an indirect band gap of 3.55 and 1.1 eV using PBEsol+U [20] with Wannier-type projectors for the *d* orbitals and HSE06 hybrid density functional calculations, respectively [18]. In contrast, the HSE06 band gaps of β-NiOOH reported by both by Zaffran et al. and Hu et al. are in the range of 1.6–2.1 eV, depending on the phase [12,15], in line with the value of 1.96 eV that was obtained by

* Corresponding author.
E-mail address: cristiana.divalentin@unimib.it (C. Di Valentin).

https://doi.org/10.1016/j.actamat.2025.121434
Received 13 May 2025; Received in revised form 22 July 2025; Accepted 11 August 2025
Available online 12 August 2025

G_0W_0 calculations [9]. Goldsmith et al. [21] stressed the importance of using hybrid functionals rather than computationally less expensive PBE+U method to obtain accurate redox potentials and thermodynamic properties and reported a band gap of 2.65 eV for a two layered NiOOH model using the PBE0 functional.

Experimentally, NiO_x is known to efficiently catalyze the Oxygen Evolution Reaction (OER) under alkaline conditions, especially when doped with Fe, which boosts its OER activity [22–24]. These experiments reported that the optimal OER performance occurs at Fe-doping concentrations of 5–50 %, with peak performance observed at around 25 %, see Table S4. However, the character of the active phase is still under debate. Multiple experiments reported that β-NiOOH exhibits superior OER activity in comparison to γ-NiOOH [25–27]. However, subsequent studies showed that those findings were due to contamination by Fe impurities and the disordered γ-NiOOH is actually more OER active than β-NiOOH [22]. The investigation of the OER active phase and mechanism faces significant issues, such as the difficulty in detecting the composition and structure of NiO_x under OER conditions, the overlap of the Ni redox peak with the OER onset potential, and the challenge of a simultaneous in-situ composition and structure detection [22–24,28–31].

The active phase and mechanism of the OER on NiOOH have been the subject of numerous DFT studies over the last years [12,21,32–36]. With regard to the OER on the Fe-doped β-NiOOH (0001) surface, only a slight or no improvement of the activity with respect to the undoped system was reported by PBE+U [37] or combined PBE+U/HSE06 [38] calculations, respectively, in disagreement with the significant boost observed in the experiments [22,23]. Using PBE+U calculations, Zhou et al. [39] instead found that the overpotential drops by 0.42 V (from 0.65 V to 0.23 V) when Fe atoms are adsorbed on the β-NiOOH (0001) surface. However, their structural model is different from that found in experiments, where Fe atoms replace Ni within the layers [23]. To explain the experimental observations, many studies considered more reactive but less stable surfaces [17,19,23,24,38]. For example, Martirez et al. predicted overpotentials of 0.48 and 0.14 V for undoped and Fe-doped β-NiOOH ($\bar{1}2\bar{1}1$) surfaces, respectively, with a reduction of 0.34 V, using a combined PBE+U/HSE06 method [19]. Using PBE+U, Li et al. examined the OER mechanism for the pure and Fe-doped β-NiOOH ($01\bar{1}5$) and γ-NiOOH (101) and estimated an overpotentials reduction of 0.20 and 0.04 V, respectively [17]. Friebel et al. calculated the overpotential for the γ-NiOOH ($01\bar{1}2$) surface with the PBE+U method, and obtained values of 0.56 and 0.43 V for the undoped and Fe-doped cases, respectively, with a reduction of 0.13 V [23]. However, although high-index facets are expected to take part in the catalytic process, the low-index (0001) facet is the most abundant and thermodynamically stable surface [12] under equilibrium conditions, as shown by DFT+U calculations and Wulff construction analysis that predict a surface energy of 0.320 J/m^2 in vacuum and 0.192 J/m^2 in aqueous environment [35,40]. The second most stable surface, the ($10\bar{1}0$) facet, exhibits much higher surface energies, 0.579 J/m^2 in vacuum and 0.445 J/m^2 in aqueous conditions [35,40]. Therefore, it is imperative to elucidate the role of the (0001) surface in the enhancement of the OER activity by Fe-doped NiOOH. Specifically, one major open question is: do Fe dopants on the most exposed surface play any role in boosting the catalytic activity of NiOOH?

It is worth noting that theoretical studies have generally overlooked the role of Fe-doping in the phase-stability of NiOOH. Experiments have shown that undoped α-$Ni(OH)_2$ is unstable in alkaline solutions and transforms to β-$Ni(OH)_2$ upon aging and to ordered β-NiOOH under applied potential [22,23,41,42]. In contrast, the introduction of substitutional Fe hinders the formation of β-NiOOH in favor of γ-NiOOH, which is characterized by a much larger interlayer spacing [22,23]. In fact, the interlayer spacing of Ni-Fe layered double hydroxides is significantly larger than that of β-$Ni(OH)_2$, because the appearance of Fe^{3+}, with a higher oxidation state than Ni^{2+}, needs to be charge compensated by the intercalation of anions and water in the interlayers [22,23]. Further experimental and theoretical studies of the Fe- induced NiOOH phase transition are needed to elucidate the actual active phase and the corresponding OER mechanism.

In this work, we present a systematic study of the atomic and electronic structures of NiOOH, as well as the OER mechanism on its (0001) surface, using the HSE06 and PBE+U methods with Grimme's D3 dispersion corrections [43,44] and full geometry optimization of the calculated structures. We confirm that, in contrast to the results obtained using PBE+U+D3, the electronic properties of NiOOH predicted by HSE06+D3 are in good agreement with the experiments. Therefore, we use the HSE06+D3 method to investigate the OER mechanism, oxidation state, chemical bonding, and phase transition energy of pure and Fe-doped NiOOH. We also test different exact exchange fractions (15 vs 25 %), since previous studies [19] suggested that a fraction of 15 % might be more suitable than the standard 25 % value for the redox behavior of undoped/Fe-doped β-NiOOH-L ($\bar{1}2\bar{1}1$) surface. Our calculations also show that Fe doping promotes the transformation from β-NiOOH to γ-NiOOH. As a result, β-NiOOH and Fe-doped γ-NiOOH are the OER active phases for pure and Fe-doped NiOOH, respectively.

2. Computational methods

Fully optimized structures, electronic properties and OER activities were investigated based on two sets of calculations. The first set of calculations used the Heyd−Scuseria−Ernzerhof (HSE06) functional [45] augmented with D3 (BJ) corrections as implemented in CRYSTAL17 code [46]. The Kohn–Sham orbitals were expanded in Gaussian-type orbitals with the POB-TZVP-REV2 all-electron basis sets. Energy convergence criterion was set to 10^{-6} Hartree, with a $3 \times 3 \times 3$ k-point grid. The second set employed the Perdew–Burke–Ernzerhof (PBE) [47] functional with Hubbard ($U = 5.5$ and 4.3 eV for Ni and Fe [12,17,37,48]) and van der Waals (vdW) D3 (BJ) corrections [43,44] as implemented in the Vienna Ab initio Simulation Package (VASP) code [49–52]. PAW pseudopotentials [53,54] were utilized with a plane-wave energy cutoff of 500 eV, a k-point spacing of 0.25 Å^{-1} and an energy convergence criterion of 10^{-6} eV.

The oxidation states of Ni and Fe in NiOOH, and Fe-doped NiOOH that will be discussed in the following paragraphs have been determined based on the atomic spin densities as computed with CRYSTAL17 code [46], an approach used in many previous theoretical studies of both bulk and surface systems [12,19,21,38,55]. In these structures, Ni and Fe cations are six-coordinated to O^{2-}/OH^- ligands, and the octahedral crystal field splits the five d-orbitals into a triply degenerate t_{2g} set and a doubly degenerate e_g set. Their occupations depend on the number of electrons in the metal center and the strength of the crystal field. In a strong crystal field, the energy splitting between the t_{2g} and e_g orbitals is large, causing electrons to first fully occupy the lower energy t_{2g} orbitals, leading to electron pairing. Conversely, in a weak crystal field, the smaller energy splitting allows electrons to occupy the higher energy e_g orbitals before pairing occurs. As a result, the strong-field scenario favors a low-spin configuration, while the weak-field scenario favors a high-spin configuration. For Fe in the low-spin case, atomic spin densities around 1 and 2 correspond to Fe^{3+} ($t_{2g}^5e_g^0$) and Fe^{4+} ($t_{2g}^4e_g^0$), respectively. In the case of high-spin, atomic spin densities around 5 and 4 correspond to Fe^{3+} ($t_{2g}^3e_g^2$) and Fe^{4+} ($t_{2g}^3e_g^1$), respectively. Similarly, for Ni in the low-spin case, atomic spin densities near 1 and 0 correspond to Ni^{3+} ($t_{2g}^6e_g^1$) and Ni^{4+} ($t_{2g}^6e_g^0$), respectively. In the high-spin configuration, atomic spin densities around 3 and 4 correspond to Ni^{3+} ($t_{2g}^5e_g^2$) and Ni^{4+} ($t_{2g}^4e_g^2$), respectively.

3. Results and discussion

3.1. Structure and stability of bulk β-NiOOH

To identify the most favorable crystal structure of β-NiOOH, we computed the relative stabilities (Table 1) of the potential candidates shown in Figure S2 using 32-atom supercell models. Our PBE+*U*+D3 results agree well with previous calculations that reported the U phase to be most stable [12]. Using the HSE06+D3 method we also computed antiferromagnetic (AFM) configurations, see Table 1. Our ferromagnetic (FM) calculations obtained with the primitive cell (Table S1) are very similar to previously reported data [12], showing that the U phase is the most favorable. However, when a larger supercell (32 atoms) is used for the structural optimization, we find that the L phase is nearly as stable as the U phase, with the AFM configurations being less stable than their FM counterparts.

3.2. NiOOH surface models

The possible structures of the (0001) surface of NiOOH were modeled using four-layer slabs containing 16 Ni atoms, which were optimized by relaxing the two topmost layers. These structures are presented in Fig. 1, where panels a,b show the four-layer slab model of the β-NiOOH (0001) surfaces for the U- and L-phases, while the model of the γ-NiOOH (0001) surface is shown in Fig. 1c. The latter was generated by further removing half of the hydrogen atoms of β-NiOOH to become $\beta\text{-NiOOH}_{x=0.5}$, for which the average oxidation state of Ni increases from +3 to +3.5, a value close to that found experimentally. This model was proposed by Friebel et al. [23] both to avoid the structural uncertainties of γ-NiOOH and because it has similar oxidation states and local bond environments for the transition metal sites as found in experiments. In this model, the intercalated species are ignored because they are not experimentally well characterized. Fig. 1d and e further shows the monolayer slab models of the U- and L-phases of β-NiOOH, which were also considered to investigate the effects of the interlayer interactions on the atomic structure. As shown by Fig. 1b and e, the structures of the monolayer and four-layer slabs are almost identical for the L phase. On the contrary, the structure of the monolayer slab is significantly different from that of the four-layer slab in the case of the U phase, as indicated by the distorted OH bonds of the former vs. the vertical OH bonds of the latter, see Fig. 1a and d.

3.3. Bulk and surface electronic structures of NiOOH

The electronic structure of the U-phase of bulk β-NiOOH (denoted β-NiOOH-U in the following) computed using the HSE06+D3 functional is shown in Figure S3a,b. These calculations predict a semiconductor with a nearly direct band gap of about 1.9 eV (VBM located at **A** and CBM between **Γ** and **A**), very close to the experimental value of 1.7–1.8 eV [9]. According to the projected density of states (PDOS), both the VBM and CBM exhibit strong mixing between Ni and O atomic states (Figure S3). The computed electronic properties for the L-phase of β-NiOOH (denoted β-NiOOH-L) are similar to those of the U phase, except for a smaller computed band gap of 1.7 eV, see Figure S3c,d. In contrast, PBE+*U*+D3 predicts a very small band gap of about 0.3 eV for β-NiOOH-U and no band gap for β-NiOOH-L, see Figure S4.

The electronic structures of the NiOOH surfaces are displayed in Fig. 2. The PDOS in Fig. 2a shows that the HSE06+D3 band gap for the β-NiOOH-U (0001) surface is very close to the bulk value in Figure S3. In contrast, the widely used PBE+*U*+D3 method predicts a band gap of only ~ 0.3 eV for the U phase in Fig. 2b (similar to that for the bulk). Even worse is the estimation for the L phase surface model in Figs. 2d, which is incorrectly predicted to be metallic by PBE+*U*+D3. On the contrary, HSE06+D3 gives a band gap of 1.7 eV for the L phase, in close agreement with experiments. Similar results are obtained for the γ-NiOOH (0001) surface, for which HSE06+D3 gives a band gap of 1.1 eV, whereas PBE+*U*+D3 predicts the system to be metallic (Figs. 2e and f).

The surface electronic properties are expected to have an important influence on the OER catalytic properties, which will be assessed in the next section. In particular, a large underestimation of the band gap may favor/disfavor certain catalytic steps and, consequently, cause a false identification of the potential determining step (PDS) and the overpotential.

3.4. Assessing the computational setup for the study of the OER mechanism on β-NiOOH

Different from previous theoretical studies that considered high-index facets to obtain lower OER overpotentials [17,19,23], in this work we focus on β-NiOOH (0001), which is the most stable and abundant surface of β-NiOOH, as identified through DFT+*U* calculations and Wulff construction analyses in both vacuum and aqueous environments [12,35,40]. As proposed by Hu et al. [12] and illustrated in Figure S5, we investigate two OER pathways on this surface, considering either an O or OH vacancy as the active site, respectively.

We first tested whether the surface monolayer model, used in previous calculations [12,21,56,57], is capable to correctly reproduce the OER free energy profile obtained with a more realistic multilayer model. From Fig. 3b and d, we can see that the OER overpotential of the L phase surface calculated using PBE+*U*+D3 has a weak dependence on the number of layers, in line with previous results [56]. This is mainly because there is only a slight structural difference between mono- and four-layer models after structural optimization, see Fig. 1b and e. For the U phase, instead, there is a clear structural difference between the mono- and four-layer models, see Fig. 1a and d. For the monolayer model, our calculations (Fig. 3a) give nearly the same OER overpotential values as those reported in a previous work [12]. On the contrary, the overpotential for the O-site changes (drops) by about 20 %, from 0.74 to 0.59 V, when we use a four-layer slab model, see Fig. 3a and c. This means that interlayer interactions cannot be ignored, hence the monolayer model is not sufficiently accurate for evaluating the OER activity. Therefore, we shall now consider only four-layer models for a more reliable discussion.

We next addressed the effect of the electronic structure method on the energetics of the OER catalytic process, as illustrated by the difference between the results in Fig. 3e and f (HSE06+D3) and Fig. 3c and d (PBE+*U*+D3). We note that for the U phase, the PBE+*U*+D3 method predicts nearly the same overpotential for both the O and OH sites, which is quite different from the HSE06+D3 results, where the O site is more favorable by ~ 0.3 V. For the L phase, PBE+*U*+D3 predicts an OER overpotential of 0.46 V at the OH site, which is also very different from the value of 0.92 V resulting from the HSE06+D3 calculations. Notably, the HSE06+D3 functional predicts the O site to be more favorable than

Table 1
Relative stability of various β-NiOOH bulk structures. Relative energies (in eV) per 32-atom supercell using the PBE+*U*+D3 and HSE06+D3 methods. Corresponding relative energies per formula unit (4 atoms) are provided in parentheses, expressed in meV. In this work all structures have been fully optimized using a 32-atom supercell model.

Methods	U	S	L	M	Reference
PBE+*U*+D3	Ferromagnetic (FM)				Ref. [12]
	0.00 (0)	0.52 (64)	0.19 (24)	0.19 (23)	
	FM				This work
	0.00 (0)	0.55 (69)	0.18 (22)	0.10 (13)	
HSE06+D3	FM				Ref. [12]
	0.00 (0)	0.59 (74)	0.23 (28)	0.39 (48)	
	FM				This work
	0.00 (0)	0.45 (56)	0.03 (3)	0.31 (38)	
	Antiferromagnetic (AFM)				
	0.01 (2)	0.34 (42)	0.07 (9)	0.33 (41)	

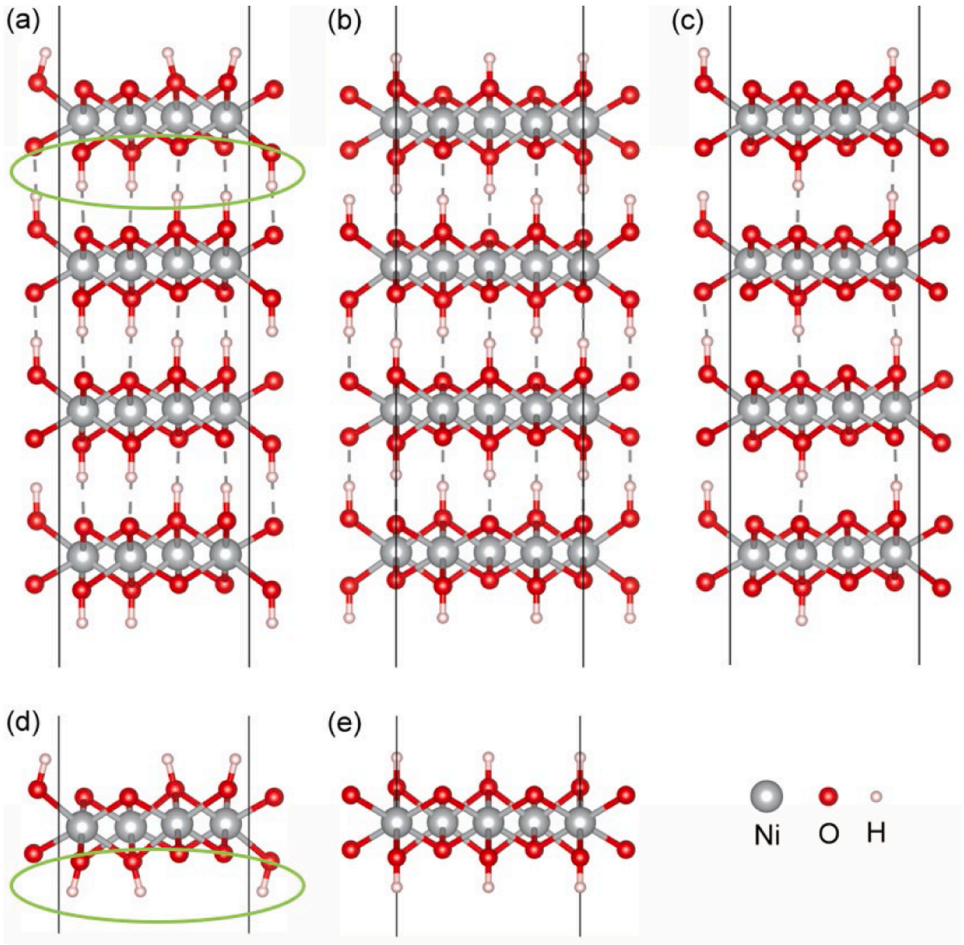

Fig. 1. The (0001) surface of the four-layer slabs of (a) U-phase β-NiOOH, (b) L-phase β-NiOOH, and (c) γ-NiOOH; and the monolayer slabs of (d) U-phase β-NiOOH and (e) L-phase β-NiOOH. The green ovals highlight the different arrangements of the H atoms in the four-layer and monolayer models of U-phase β-NiOOH.

the OH site. An OER reaction at an O site is consistent with experiments [58] showing that during electrocatalytic oxidation single H defects are formed due to dehydrogenation, and allows for a cyclic conversion between $Ni(OH)_2$ and NiOOH, while the OH site does not. Moreover, our HSE06+D3 calculations predict similar OER free energy profiles for the surfaces of the U and L phases, whereas very different OER overpotentials are obtained for these two phases using the PBE+*U*+D3 method, likely because PBE+*U*+D3 predicts the U phase to be semiconducting and the L phase metallic, see Fig. 2b and d. Hence, these comparisons indicate that more expensive but accurate HSE06+D3 calculations are crucial to reliably describe the OER mechanism of β-NiOOH.

Finally, we studied the effect of different magnetic configurations on the OER mechanism, see Fig. 3e and f (FM) and S6 (AFM). Figure S6 shows that for both the U and L phases the OER mechanisms and overpotentials of the AFM configurations are similar to those of the FM configurations in Fig. 3e and f. In particular, the O-O coupling step 3 ($*O + OH^- \rightarrow *OOH + e^-$) is the PDS at the O site, which is more favorable for the OER than the OH site. Overall, the OER mechanism is largely independent from the magnetic configurations. Therefore, in the following section, only the more stable FM configuration is considered.

3.5. OER mechanism for pure and Fe-doped β-NiOOH

In this section, we investigate the OER activity of β-NiOOH (0001), with a 25 % doping concentration of Fe atoms in the top surface layer, as shown in Fig. 4 and Table 2. We first determine the most favorable substitutional site for the Fe dopant and then evaluate the free energy profile of the OER catalytic process (Fig. 4). Although more sophisticated methodologies providing accurate insights into OER reactivity are available [59], here we use the computational hydrogen electrode (CHE) model[40]. This simplified approach is justified because we are focusing on trends, going from pure to doped system, rather than on absolute overpotential values. Similarly, solvation contributions to the free energies of the reaction intermediates along the OER pathway were not included, because the results of a previous study [12] show that the effect of the water solvent on the OER overpotential does not exceed 0.03 V. Thus, this effect can be safely neglected in the present work.

Fig. 4a indicates that the PDS for undoped β-NiOOH (0001) is the O-O coupling step 3 ($*O + OH^- \rightarrow *OOH + e^-$). The computed overpotential is 0.68 V, a value within the experimental range of 0.57–0.68 V [23,24]. Fe doping (Fig. 4b) does not change the PDS but decreases the overpotential to 0.56 V, with a reduction of 0.12 V, larger than that of 0.07 V reported by previous PBE+*U* calculations [37] but still significantly smaller than the experimental value of 0.31 V reported by Friebel et al. [23] and 0.23 V by Dionigi et al. [24]. Incidentally, we note that the small value of the computed overpotential decrease is the reason why many computational studies examined less stable high-index surfaces, such as $(01\bar{1}5)$ and $(01\bar{1}2)$, and γ-NiOOH, which usually provide lower OER potentials [17,23] but are also less stable and less abundant than the (0001) facet.

3.6. OER mechanism for pure and Fe-doped γ-NiOOH

Our results for γ-NiOOH, another potential active phase for the OER are reported in Fig. 4c and d and Table 2. In comparison to β-NiOOH,

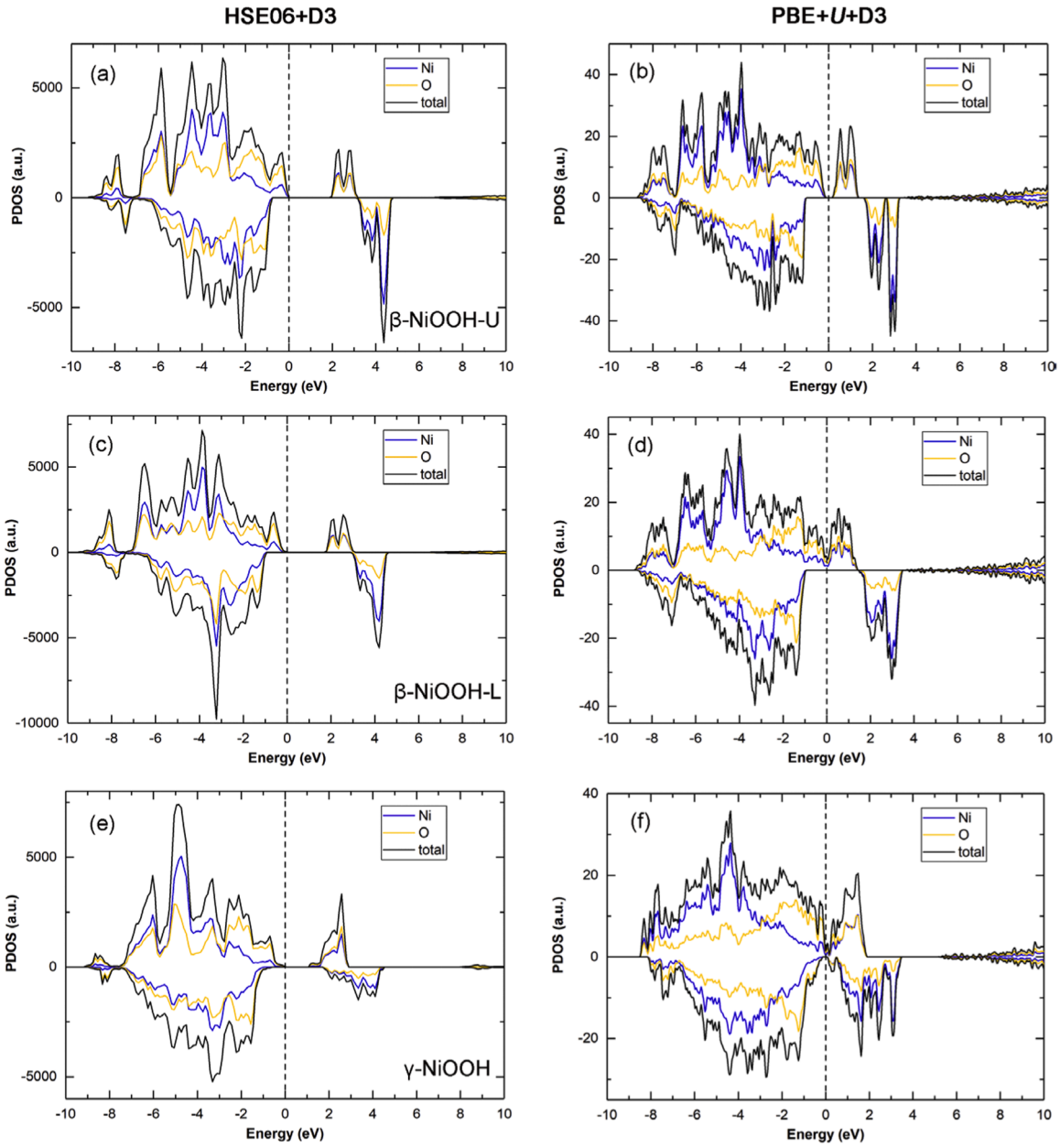

Fig. 2. PDOS for the (0001) surfaces of β-NiOOH-U (a,b), β-NiOOH-L (c,d), and γ-NiOOH (e,f), calculated using four-layer slab models with HSE06+D3 (left) and PBE+U + D3 (right), respectively. The energy zero corresponds to the Fermi energy (or top of the valence band in semiconducting systems).

γ-NiOOH exhibits a lower OER overpotential of 0.51 V, with step 2 (*OH + OH^- → *O + H_2O + e^-) as the PDS. Fe-doping further decreases the overpotential to 0.45 V, with a reduction of 0.06 V relative to the undoped case. Therefore, the phase transition from β-NiOOH to γ-NiOOH has a significant effect on the overpotential, which decreases from 0.68 V to 0.51 V, while Fe doping further reduces the overpotential of γ-NiOOH to 0.45 V. Importantly, it is known from experiments that Fe doping stabilizes γ-NiOOH [22,23].

Comparing the overpotential of β-NiOOH (0.68 V) with that of Fe-doped γ-NiOOH (0.45 V), it appears that the drop is quite substantial, 0.23 V. This value is in excellent agreement with the experimental results by Dionigi et al. [24], who reported that the OER overpotential of a 25 % Fe-doped α-$Ni(OH)_2$/γ-NiOOH film (0.348 eV, where α-$Ni(OH)_2$ is the starting phase that transforms into γ-NiOOH upon charging) is 0.23 V lower than that of a pure β-$Ni(OH)_2$/β-NiOOH sample (0.573 V) [24]. The overpotential drop from β-NiOOH (0001) to Fe-doped γ-NiOOH (0001) has also been confirmed by a set of HSE06(α=15 %)+D3 calculations, also considering full atomic relaxation (see Figures S7 and S8). Moreover, the presence of intercalated water has little effect on the calculated overpotential, which becomes 0.41 V (Figure S9a) compared to 0.45 V for the 'dry' Fe-doped γ-NiOOH (Figure S9b or Fig. 4d), proving the reliability of the 'dry' γ-NiOOH model [23]. Based on the analysis above, we suggest the possibility that Fe doping induces a transition from β- to γ-NiOOH under OER conditions, so that the OER active phase is β-NiOOH for the pristine sample but transforms into γ-NiOOH for the Fe-doped one. This hypothesis is consistent with X-ray diffraction (XRD) experiments showing that the introduction of Fe favors the formation of γ-NiOOH [22,23]. It is also strongly supported by the computational analysis of the oxidation state, chemical bonding and phase transition energy reported below and in the SI.

3.7. *Spin configuration and oxidation state*

We determined the oxidation states of the transition metal atoms

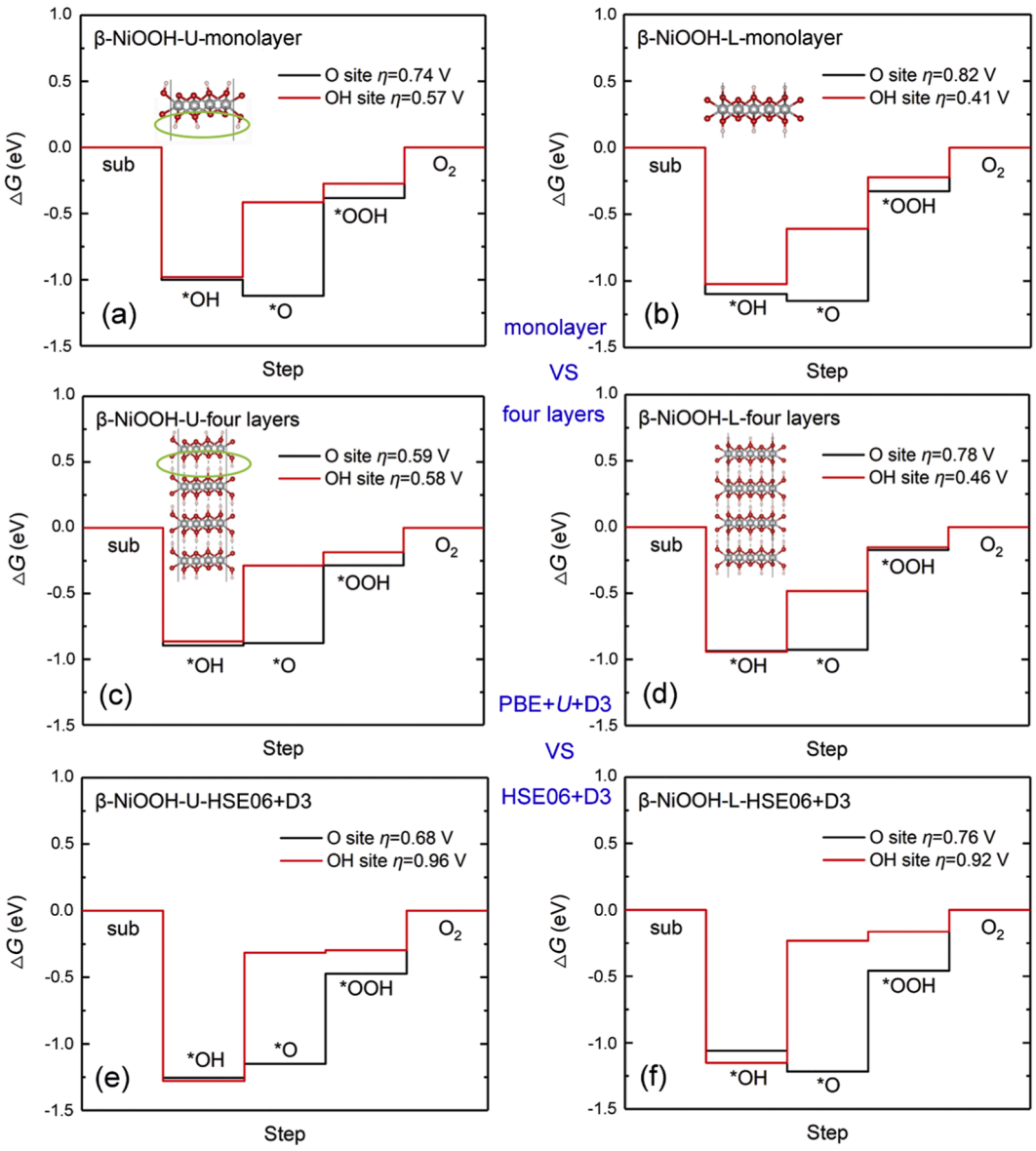

Fig. 3. Free energy profiles for the four-step OER mechanism at the O and OH active sites of β-NiOOH-U (left panels) and β-NiOOH-L (right panels): (a,b) calculated using PBE+*U*+D3 with a monolayer model of β-NiOOH (0001); (c,d) calculated using PBE+*U*+D3 with a four-layer model of β-NiOOH (0001); (e,f) calculated using HSE06+D3 with a four-layer model of β-NiOOH (0001).

based on their magnetic moments, which can be easily identified in the localized basis set used by the CRYSTAL17 code [46], as described in the Computational Details section above. With this approach, we found that all the four Ni cations in the top layer of the pristine β-NiOOH-U (0001) surface are Ni^{3+} in a low-spin d^7 configuration, see Fig. 5. For Fe-doped β-NiOOH with Fe in the top layer, one Ni^{3+} is preferably substituted by a Fe^{3+} in a high-spin (HS) d^5 configuration, which is found to be more stable than the low-spin (LS) d^5 configuration by 0.58 eV using HSE06+D3. The HS has also been computed to be the lowest energy solution for Fe-doped β-NiOOH-L (0001), $(10\bar{1}0)$ and $(\bar{1}2\bar{1}1)$ surfaces by PBE+*U*, HSE06 and PBE0, respectively [19,21,38]. On the contrary, the LS state was recently proposed for low concentrations of Fe-doping in bulk β-NiOOH-L (12.5 % per layer of NiOOH), based on PBEsol+*U* calculations with Wannier-type projectors [18], in line with previous PBE0 (α=0.15) results by Conesa [55]. As mentioned in the introduction, PBEsol+*U* predicts a larger band gap of 3.6 eV for β-NiOOH in comparison to hybrid functionals and the G_0W_0 method. Given this discrepancy in the spin state energy order, we performed additional calculations for lower Fe concentration (12.5 % instead of 25 %) by doubling the size of the supercell surface model, see Table S2. However, the HS-LS energy difference remained almost unchanged (0.61 eV).

Since the spin state is expected to affect the size of the ion, we compare, as it was previously done in Ref. [18], the Shannon ionic radii of six-fold coordinated Ni^{3+} and Fe^{3+} cations in Fe-doped β-NiOOH in both LS and HS states. Given that the size of Ni^{3+} LS state is 0.56 Å, and the ionic radii of LS and HS Fe^{3+} are 0.55 Å and 0.65 Å, respectively, it was proposed by He et al. [18] that substitutional Fe^{3+} in LS state is favored, which may also explain the large Fe solubility limit observed in experiments. However, it was reported that in the experimental samples Fe^{3+} substitutes Ni^{2+} in $Ni(OH)_2$, whose radius is 0.69 Å, and not a Ni^{3+} cation [22,23]. The introduction of Fe^{3+} with a higher oxidation state than Ni^{2+} needs to be compensated by the intercalation of anions and water in the interlayers, resulting in an interlayer spacing much larger (by 43 %) than in β-$Ni(OH)_2$. Therefore, the presence of Fe disfavors the formation of β-NiOOH after charging, favoring instead the formation of γ-NiOOH [22,23]. It is not relevant to compare the ionic radii of Ni^{3+} and Fe^{3+} cations in Fe-doped β-NiOOH [18] both because of the Fe-induced transition of NiOOH to the γ phase and because NiOOH is

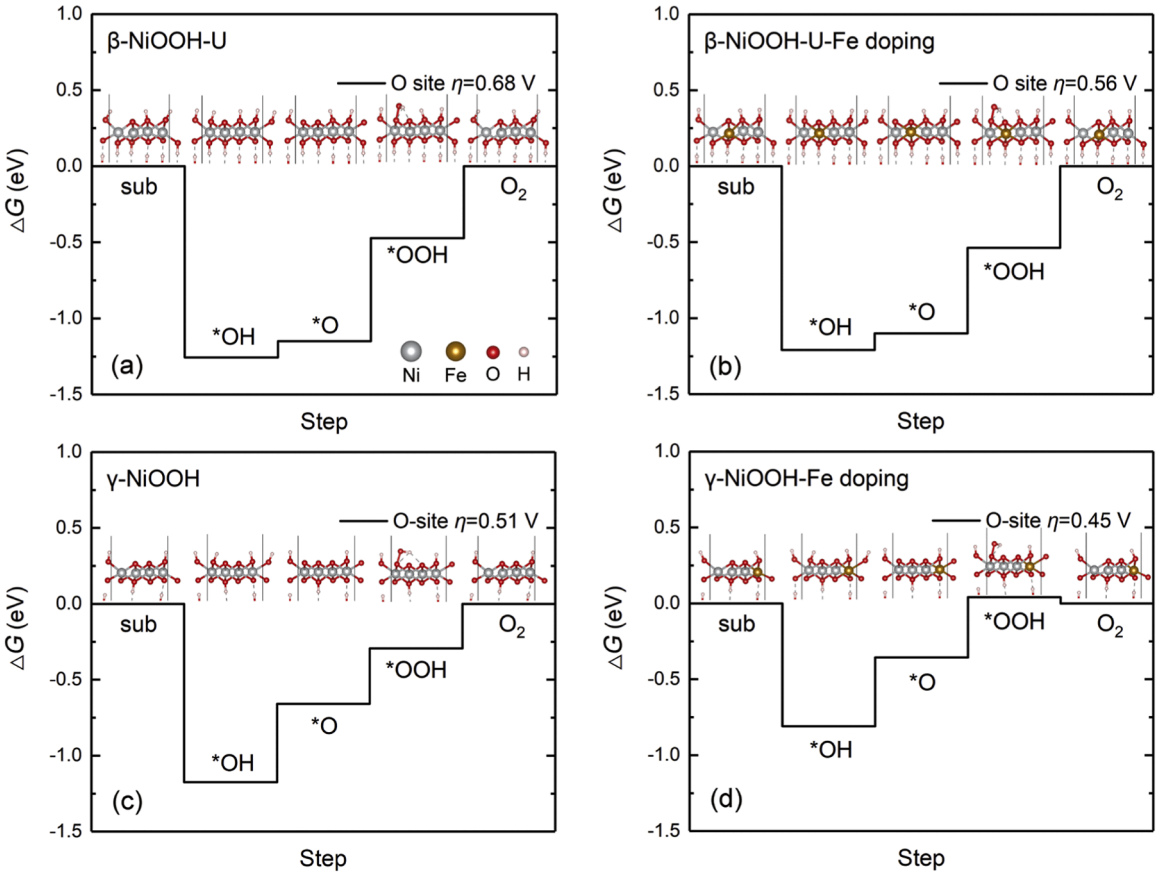

Fig. 4. OER free energy profile calculated using the HSE06+D3 method on a four-layer slab model: (a) and (b) β-NiOOH-U (0001) surface without/with 25 % Fe doping, (c) and (d) γ-NiOOH(0001) surface without/with 25 % Fe doping. In all cases, the reaction starts at an O vacancy site.

Table 2
Reaction free energies of the four steps of the OER at the O site of undoped and 25 % Fe-doped β-NiOOH-U and γ-NiOOH (0001) surface calculated using the HSE06+D3 method.

	Step	Equation	Reaction free energy (eV)
β-NiOOH-U	1	$sub + OH^- \rightarrow *OH + e^-$	−0.03
	2	$*OH + OH^- \rightarrow *O + H_2O + e^-$	1.34
	3	$*O + OH^- \rightarrow *OOH + e^-$	1.91 (η = 0.68)
	4	$*OOH + OH^- \rightarrow sub + O_2 + H_2O + e^-$	1.70
Fe-doped β-NiOOH-U	1	$sub + OH^- \rightarrow *OH + e^-$	0.02
	2	$*OH + OH^- \rightarrow *O + H_2O + e^-$	1.34
	3	$*O + OH^- \rightarrow *OOH + e^-$	1.79 (η = 0.56)
	4	$*OOH + OH^- \rightarrow sub + O_2 + H_2O + e^-$	1.77
γ-NiOOH	1	$sub + OH^- \rightarrow *OH + e^-$	0.06
	2	$*OH + OH^- \rightarrow *O + H_2O + e^-$	1.74 (η = 0.51)
	3	$*O + OH^- \rightarrow *OOH + e^-$	1.60
	4	$*OOH + OH^- \rightarrow sub + O_2 + H_2O + e^-$	1.52
Fe-doped γ-NiOOH	1	$sub + OH^- \rightarrow *OH + e^-$	0.42
	2	$*OH + OH^- \rightarrow *O + H_2O + e^-$	1.68 (η = 0.45)
	3	$*O + OH^- \rightarrow *OOH + e^-$	1.63
	4	$*OOH + OH^- \rightarrow sub + O_2 + H_2O + e^-$	1.19

produced from $Ni(OH)_2$ upon charging [22,23]. Instead, a more meaningful comparison is that of the ionic radii of Ni^{2+} and Fe^{3+} cations in Fe-doped $Ni(OH)_2$, which are 0.69 Å for low-spin Ni^{2+} and 0.65 Å for high-spin Fe^{3+}. This well explains the large concentrations of Fe reported in $Ni(OH)_2$/NiOOH films and supports the occurrence of the HS state for Fe^{3+} in $Ni(OH)_2$.

As for the γ-NiOOH phase, our model contains two Ni^{3+} and two Ni^{4+} ions in the top layer, both in the LS configurations. Different from previous RPBE+*U* calculations [23], our HSE06+D3 results show that for Fe-doped γ-NiOOH, the substitution of a Ni^{4+} ion by Fe^{4+} in a HS d^4 configuration is about 44 meV more stable than replacing a Ni^{3+} by HS Fe^{3+} in the top layer. This is consistent with previous hybrid B3PW91 and PBE0 density functional calculations [21,60], as well as with experimental Mössbauer spectroscopy results [22,61,62].

To get deeper structural insight, we also analyzed the M-O bond lengths (*M* = Fe or Ni), reported in Table S2, at different Fe concentration, spin/oxidation states and compared this data with previous computational studies [18] and with experiments [23]. The Fe and Ni coordination is characterized by four shorter and two longer M-O bonds; therefore, we present an average M-O distance based on all six values or on only the four shortest ones, as previously done in Ref. [18]. From the comparison with experiments [23], we conclude that the best fit is for Fe^{4+} in the HS configuration of γ-NiOOH.

In summary, for both Fe-doped β-NiOOH or γ-NiOOH, our calculations show that Fe cations prefer a high-spin state, which is consistent with most experimental and theoretical studies [19,21,37,38,60–63]. Moreover, our calculations indicate Ni^{3+} and Fe^{3+} are preferred in Fe-doped β-NiOOH, while Ni^{3+}, $Ni^{4+}$and Fe^{4+} oxidation states are preferred in Fe-doped γ-NiOOH. The appearance of Ni^{4+} and Fe^{4+} states, together with the bond lengths of Fe-O and Ni-O (Table S2) and also the OER overpotential (Fig. 4d) of Fe-doped γ-NiOOH agree well with the experimental observation of Ni^{4+} and Fe^{4+} cations appearing in Fe-doped NiOOH at OER potentials and are crucial for the efficient OER [21,22,24,61,62]. However, we also point out that HERFD XAS measurements indicate a low concentration of Fe^{4+} ions [23], which is different from the Mössbauer results showing the presence of a

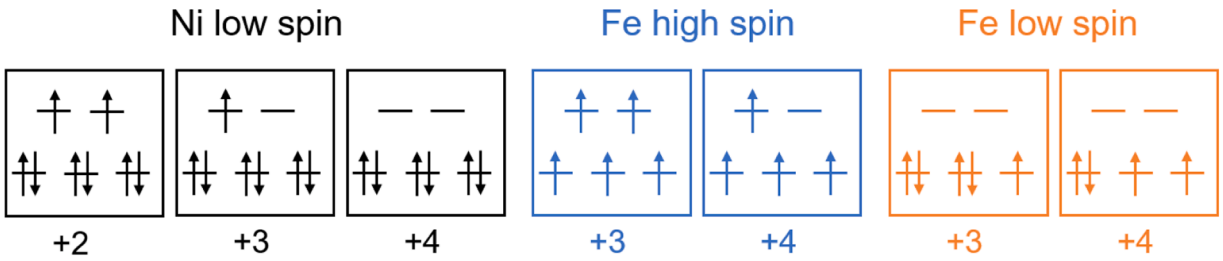

Fig. 5. The 3*d* orbital distributions of Ni and Fe cations and corresponding oxidation states for different spin configurations. Most studies indicate that the low-spin Ni and high-spin Fe cations are most stable [19,21,37,38,60–63], whereas the low-spin configuration of Fe cations was recently proposed [18] to justify the high Fe concentrations that can be experimentally observed [23].

significant amount of Fe^{4+} cations under OER conditions, which are crucial for the efficiency of the OER [22,61,62].

3.8. Chemical bonding

In Fig. 6 we show the atomic structures of the undoped and 25 % Fe-doped β-NiOOH surface models. Doping results in shorter M-O (M = Ni and Fe) bond lengths, from 2.04 Å in the undoped structure to 1.94 Å in the Fe-doped one (see atomic labels in Fig. 6). In contrast, the O-H bond length increases from 1.02 Å to 1.05 Å. Further details of the effect of doping on the bonds in β-NiOOH are provided by calculating the crystal orbital Hamilton populations (COHP) and energy-integrated COHP (ICOHP) using LOBSTER 5.0.0 [64–70] (see S.I.). The COHP method analyzes the interactions between atoms by partitioning the band-structure energy into bonding, nonbonding and antibonding contributions, by also taking into account the wavefunctions' phase information, thus going *beyond* the simple DOS. The ICOHP provides an indication of the bond energy (or strength) up to the Fermi level, including all populated levels: the more negative ICOHP values, the stronger the covalent bond [64–70].

In Fig. 6, the COHP chemical-bonding analysis of the M-O and O-H bonds (labeled in the inset panels of Fig. 6) is shown for the undoped and Fe-doped systems. Covalent bonding interactions are negative (because they lower the energy), and for reasons of convenience, we plot −COHP such that all bonding interactions are on the right and antibonding on the left, a simple graphical convention. Additionally, since our systems are spin polarized, spin-up (majority) and spin-down (minority) components are treated separately.

Starting with the undoped case (Fig. 6a), for the Ni-O bond there is a majority (α, in blue) occupied antibonding state below the Fermi level, whereas no minority (β, in orange) occupied antibonding components are present. This is a consequence of the exchange hole, which makes the α/β spin orbitals more/less contracted. Because of that, the computed minority ICOHP value (−1.01 eV) is more than twice as bonding compared to the majority value (−0.46 eV), for reasons well known [71]. Moving to the Fe-doped system (Fig. 6b) and considering the Fe-O bond, the occupied bonding levels clearly outperform the occupied antibonding levels, making the ICOHP values for both majority (α, in blue) and minority (β, in orange) levels more bonding compared to the undoped case. Therefore, the covalent contribution to the Fe-O bonds is stronger than for the Ni-O bonds, in line with the shorter bond distance.

For the O-H bond (Fig. 6c and d), the trend is reversed. The covalent part of the O-H bond is stronger in the undoped system than in the Fe-doped case, as reflected in the ICOHP values obtained by summing up the majority/minority levels: −4.11 eV − 4.14 eV = −8.25 eV for Fe-O vs. −3.83 eV − 3.85 eV = −7.88 eV for Ni-O. Hence, Fe doping strengthens the Fe-O bond at the expense of the O-H bond. As a result, Fe doping promotes the phase transformation from β-NiOOH to γ-NiOOH, as confirmed by the computed phase transition energy in Table 3.

3.9. Free energy of phase transition

The phase transition free energy from β-NiOOH to γ-NiOOH was computed according to the equation: $\Delta G_{pt} = G_{H2,(g)} + G_{\gamma\text{-NiOOH}} - G_{\beta\text{-}}$

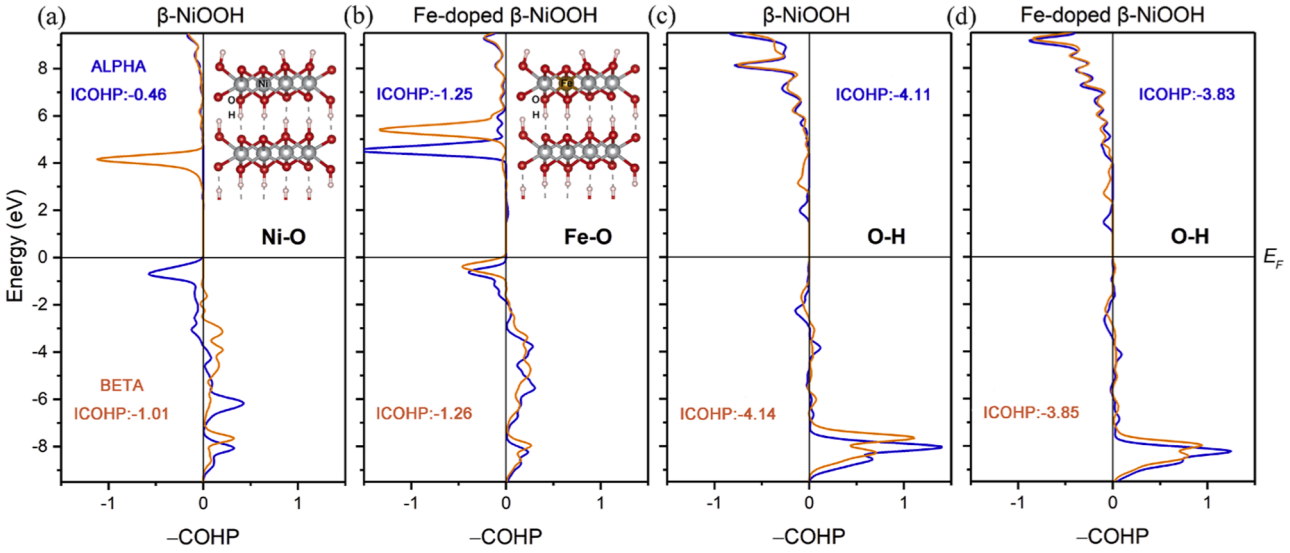

Fig. 6. Chemical bonding analysis of (a) Ni-O and (c) O-H bonds in the top layer of the (0001) surface of β-NiOOH and (b) Fe-O and (d) O-H bonds at the corresponding sites of Fe-doped systems by COHP and ICOHP (eV) of HSE06+D3 results. The energy zero corresponds to the Fermi energy (or top of the valence band in semiconducting systems), and by plotting negative COHP all bonding/antibonding interactions go to the right/left. Blue and orange curves are for spin-up and spin-down states, respectively.

Table 3
Free energy of phase transition (ΔG_{pt}) from β-NiOOH to γ-NiOOH (top layer) with and without doping in oxygenated environment by HSE06+D3 method.

β-NiOOH + ½ $O_{2,(g)}$ → γ-NiOOH (top layer) + $H_2O_{,(l)}$	ΔG_{pt} (eV/H_2O)	$\Delta\Delta G_{pt}$ (eV/H_2O)
γ-NiOOH	2.059	–
Fe-doped γ-NiOOH	1.864	−0.195

$_{NiOOH}$, where $G_{H2,(g)}$, $G_{\gamma\text{-NiOOH}}$ and $G_{\beta\text{-NiOOH}}$ are the free energies of H_2 (in the gas phase), γ-NiOOH and β-NiOOH, respectively. Here we removed two H atoms from the top layer of β-NiOOH to form γ-NiOOH (top layer) to keep consistency with the doping effect that was investigated only for the top layer of a four-layer model. We considered two reaction conditions: vacuum and oxygenated conditions.

In vacuum, the reaction involves the direct deprotonation and oxidation of the top layer of β-NiOOH to form a top layer of γ-NiOOH and one H_2 molecule (gas phase), with the lower three layers of the slab model unmodified. Table S3 shows that Fe doping decreases ΔG_{pt} from +4.519 eV for undoped NiOOH to +4.324 eV for Fe-doped NiOOH.

More realistically, the formation of γ-NiOOH (top layer) takes place in an oxygenated environment according to the following equation:

$$\beta - \mathrm{NiOOH} + 1/2\ \mathrm{O}_{2,(g)} \rightarrow \gamma - \mathrm{NiOOH(top\ layer)} + \mathrm{H_2O}_{,(l)}.$$

Interestingly, the oxygen environment significantly lowers ΔG_{pt} from +4.519 to +2.059 eV in the case of the undoped system, see Tables 3 and S2. Fe doping further decreases ΔG_{pt} to +1.864 eV, a reduction of 9 % (Table 3), suggesting that Fe doping promotes the formation of γ-NiOOH from β-NiOOH, even though ΔG_{pt} is still positive. The positive phase transition energy is because the formation of γ-NiOOH requires an applied voltage (electric potential) to enable this transition, which is lower in the case of the Fe-doped system. Another contribution comes from the pH. In particular the transformation is promoted at high pH values (alkaline conditions).

4. Conclusions

In this work, we have systematically studied the atomic and electronic structures of NiOOH and the OER mechanism at the (0001) surface by the HSE06+D3 and PBE+*U*+D3 methods. According to our calculations and in agreement with previous studies [9,15,17–19], PBE+*U*+D3 predicts a very small band gap and even metallic properties for NiOOH, in conflict with experiments [13]. We confirmed that this inconsistency is solved by the HSE06+D3 method. Differently from PBE+*U*+D3, HSE06+D3 predicts that the OER preferentially occurs at an O site (rather than at an OH site), where it allows a cyclic conversion between $Ni(OH)_2$ and NiOOH, that is consistent with experimental observations [58]. Using HSE06+D3, we also studied the effect of Fe doping on the oxidation state, chemical bonding, phase transition energy and OER of NiOOH. Our calculations reveal that Fe doping weakens the adjacent O-H bonds, hence it can promote the β-NiOOH to γ-NiOOH transformation, in line with the experimental observations [22,23] that (i) the presence of Fe prevents formation of β-$Ni(OH)_2$/β-NiOOH, and (ii) the formed Fe-doped films have a much larger interlayer spacing than β-$Ni(OH)_2$/β-NiOOH, with the typical character of α-$Ni(OH)_2$/γ-NiOOH. That is to say, β-NiOOH is the OER active phase for the undoped phase, with a calculated overpotential of 0.68 V, that is very close to the experimental value [23]. With regard to the Fe doped films, γ-NiOOH is predicted to be the OER active phase with an overpotential value of 0.45 V, which is also close to experiments [23]. Remarkably, the lowering of our calculated OER overpotential from β-NiOOH to Fe-doped γ-NiOOH (0.68 → 0.45 V) agrees very well with the experimental drop of 0.23 V measured by Dionigi et al. [24] from undoped β-$Ni(OH)_2$/β-NiOOH to 25 % Fe-doped α-$Ni(OH)_2$/γ-NiOOH film. This finding is also supported by our oxidation-state analysis. Different from previous RPBE+*U* calculations [23], our HSE06+D3 results indicate that Fe^{4+} cations are more favorable than Fe^{3+} in γ-NiOOH, consistent with the experimental (including Mößbauer) evidence [21,22,24,61,62] that Fe^{4+} cations are formed during the OER process and are crucial for an efficient OER. In conclusion, our study strongly suggests that the phase transition induced by Fe doping is key to effectively achieve a lower OER overpotential for NiOOH. This finding, based on detailed calculations of experimentally relevant quantities, sheds light on the long-standing debate about the OER mechanism and active phase of NiOOH.

Supporting information

Calculation details, crystal structure, phase stability, band structure and PDOS, OER pathway, OER diagram, bond length, phase transition energy.

Data availability

The data that support the conclusions in this study are present in the paper and the Supplementary materials and are available from the corresponding author upon reasonable request.

CRediT authorship contribution statement

Da Chen: Writing – original draft, Visualization, Investigation, Formal analysis, Data curation. **Daniele Perilli:** Validation, Formal analysis. **Richard Dronskowski:** Writing – review & editing, Formal analysis. **Annabella Selloni:** Writing – review & editing, Formal analysis. **Cristiana Di Valentin:** Writing – review & editing, Supervision, Resources, Project administration, Funding acquisition, Formal analysis, Conceptualization.

Declaration of competing interest

The authors declare that they have no known competing financial interests or personal relationships that could have appeared to influence the work reported in this paper.

Acknowledgements

The authors thank Lorenzo Ferraro and Dr. Chiara Daldossi for technical support and helpful discussions on the calculations, and Prof. Laura Calvillo Lamana for valuable discussions on experiments. The authors thank the support of the high-performance computing resources of University of Milano-Bicocca and Hoffmann Institute of Advanced Materials at Shenzhen Polytechnic University. D.P. and C.D.V. acknowledge funding from the European Union-NextGenerationEU through the Italian Ministry of University and Research under PNRR-M4C2I1.4 ICSC-Centro Nazionale di Ricerca in High-Performance Computing, Big Data and Quantum Computing (grant no. CN00000013). This work has been supported by the project "Hydrogen, electricity, and clean water from recycled nickel and urea" funded by the MIUR Progetti di Ricerca di Rilevante Interesse Nazionale (PRIN 2022 PNRR-M4C2I1.1) - Grant P2022FALAP.

Supplementary materials

Supplementary material associated with this article can be found, in the online version, at doi:10.1016/j.actamat.2025.121434.

References

[1] H. Bode, K. Dehmelt, J. Witte, Zur kenntnis der nickelhydroxidelektrode—I. Über das nickel (II)-hydroxidhydrat, Electrochim. Acta 11 (8) (1966) 1079–1087.
[2] H. Bode, K. Dehmelt, J. Witte, Zur Kenntnis der Nickelhydroxidelektrode. II. Über die Oxydationsprodukte von Nickel (ii)-hydroxiden, Z. Anorg. Allg. Chem. 366 (1–2) (1969) 1–21.
[3] C. Tessier, P. Haumesser, P. Bernard, C. Delmas, The structure of $Ni(OH)_2$: from the ideal material to the electrochemically active one, J. Electrochem. Soc. 146 (6) (1999) 2059.

[4] Q. Song, Z. Tang, H. Guo, S. Chan, Structural characteristics of nickel hydroxide synthesized by a chemical precipitation route under different pH values, J. Power Sources 112 (2) (2002) 428–434.
[5] R. Barnard, C. Randell, F. Tye, Studies concerning charged nickel hydroxide electrodes I. Measurement of reversible potentials, J. Appl. Electrochem. 10 (1980) 109–125.
[6] F. Portemer, A. Delahaye-Vidal, M. Figlarz, Characterization of active material deposited at the nickel hydroxide electrode by electrochemical impregnation, J. Electrochem. Soc. 139 (3) (1992) 671.
[7] S. Park, Y. Lee, M. Elcombe, T. Vogt, Synthesis and structure of the bilayer hydrate $Na_{0.3}NiO_2{\cdot}1.3D_2O$, Inorg. Chem. 45 (9) (2006) 3490–3492.
[8] X. Yang, K. Takada, M. Itose, Y. Ebina, R. Ma, K. Fukuda, T. Sasaki, Highly swollen layered nickel oxide with a trilayer hydrate structure, Chem. Mater. 20 (2) (2008) 479–485.
[9] A.J. Tkalych, K. Yu, E.A. Carter, Structural and electronic features of β-$Ni(OH)_2$ and β-NiOOH from first principles, J. Phys. Chem. C 119 (43) (2015) 24315–24322.
[10] P. Oliva, J. Leonardi, J. Laurent, C. Delmas, J. Braconnier, M. Figlarz, F. Fievet, A. De Guibert, Review of the structure and the electrochemistry of nickel hydroxides and oxy-hydroxides, J. Power Sources 8 (2) (1982) 229–255.
[11] V.Y. Kazimirov, M. Smirnov, L. Bourgeois, L. Guerlou-Demourgues, L. Servant, A. Balagurov, I. Natkaniec, N. Khasanova, E. Antipov, Atomic structure and lattice dynamics of Ni and Mg hydroxides, Solid State Ion 181 (39–40) (2010) 1764–1770.
[12] Q. Hu, Y. Xue, J. Kang, I. Scivetti, G. Teobaldi, A. Selloni, L. Guo, L.-M. Liu, Structure and oxygen evolution activity of β-NiOOH: where are the protons? ACS Catal 12 (1) (2021) 295–304.
[13] M.K. Carpenter, D.A. Corrigan, Photoelectrochemistry of nickel hydroxide thin films, J. Electrochem. Soc. 136 (4) (1989) 1022.
[14] A. Varkey, A. Fort, Solution growth technique for deposition of nickel oxide thin films, Thin Solid Films 235 (1–2) (1993) 47–50.
[15] J. Zaffran, M.Caspary Toroker, Benchmarking density functional theory based methods to model NiOOH material properties: hubbard and van der Waals corrections vs hybrid functionals, J. Chem. Theory Comput. 12 (8) (2016) 3807–3812.
[16] E.L. Ratcliff, J. Meyer, K.X. Steirer, A. Garcia, J.J. Berry, D.S. Ginley, D.C. Olson, A. Kahn, N.R. Armstrong, Evidence for near-surface NiOOH species in solution-processed NiOx selective interlayer materials: impact on energetics and the performance of polymer bulk heterojunction photovoltaics, Chem. Mater. 23 (22) (2011) 4988–5000.
[17] Y.-F. Li, A. Selloni, Mechanism and activity of water oxidation on selected surfaces of pure and Fe-doped NiOx, ACS Catal 4 (4) (2014) 1148–1153.
[18] Z.-D. He, R. Tesch, M.J. Eslamibidgoli, M.H. Eikerling, P.M. Kowalski, Low-spin state of Fe in Fe-doped NiOOH electrocatalysts, Nat. Commun. 14 (1) (2023) 3498.
[19] J.M.P. Martirez, E.A. Carter, Unraveling oxygen evolution on iron-doped β-nickel oxyhydroxide: the key role of highly active molecular-like sites, J. Am. Chem. Soc. 141 (1) (2018) 693–705.
[20] J.P. Perdew, A. Ruzsinszky, G.I. Csonka, O.A. Vydrov, G.E. Scuseria, L. A. Constantin, X. Zhou, K. Burke, Restoring the density-gradient expansion for exchange in solids and surfaces, Phys. Rev. Lett. 100 (13) (2008) 136406.
[21] Z.K. Goldsmith, A.K. Harshan, J.B. Gerken, M. Vörös, G. Galli, S.S. Stahl, S. Hammes-Schiffer, Characterization of NiFe oxyhydroxide electrocatalysts by integrated electronic structure calculations and spectroelectrochemistry, Proc. Natl Acad. Sci. USA 114 (12) (2017) 3050–3055.
[22] L. Trotochaud, S.L. Young, J.K. Ranney, S.W. Boettcher, Nickel–iron oxyhydroxide oxygen-evolution electrocatalysts: the role of intentional and incidental iron incorporation, J. Am. Chem. Soc. 136 (18) (2014) 6744–6753.
[23] D. Friebel, M.W. Louie, M. Bajdich, K.E. Sanwald, Y. Cai, A.M. Wise, M.-J. Cheng, D. Sokaras, T.-C. Weng, R. Alonso-Mori, Identification of highly active Fe sites in (Ni, Fe)OOH for electrocatalytic water splitting, J. Am. Chem. Soc. 137 (3) (2015) 1305–1313.
[24] F. Dionigi, Z. Zeng, I. Sinev, T. Merzdorf, S. Deshpande, M.B. Lopez, S. Kunze, I. Zegkinoglou, H. Sarodnik, D. Fan, In-situ structure and catalytic mechanism of NiFe and CoFe layered double hydroxides during oxygen evolution, Nat. Commun. 11 (1) (2020) 2522.
[25] P. Lu, S. Srinivasan, Electrochemical-ellipsometric studies of oxide film formed on nickel during oxygen evolution, J. Electrochem. Soc. 125 (9) (1978) 1416.
[26] M. Wehrens-Dijksma, P. Notten, Electrochemical Quartz microbalance characterization of $Ni(OH)_2$-based thin film electrodes, Electrochim. Acta 51 (18) (2006) 3609–3621.
[27] I. Godwin, M. Lyons, Enhanced oxygen evolution at hydrous nickel oxide electrodes via electrochemical ageing in alkaline solution, Electrochem. commun. 32 (2013) 39–42.
[28] M.E. Lyons, M.P. Brandon, The oxygen evolution reaction on passive oxide covered transition metal electrodes in aqueous alkaline solution. Part 1-nickel, Int. J. Electrochem. Sci. 3 (12) (2008) 1386–1424.
[29] D.K. Bediako, B. Lassalle-Kaiser, Y. Surendranath, J. Yano, V.K. Yachandra, D. G. Nocera, Structure–activity correlations in a nickel–borate oxygen evolution catalyst, J. Am. Chem. Soc. 134 (15) (2012) 6801–6809.
[30] M. Gong, H. Dai, A mini review of NiFe-based materials as highly active oxygen evolution reaction electrocatalysts, Nano Res. 8 (2015) 23–39.
[31] S. Klaus, Y. Cai, M.W. Louie, L. Trotochaud, A.T. Bell, Effects of Fe electrolyte impurities on $Ni(OH)_2$/NiOOH structure and oxygen evolution activity, J. Phys. Chem. C 119 (13) (2015) 7243–7254.
[32] A. Govind Rajan, J.M.P. Martirez, E.A. Carter, Facet-independent oxygen evolution activity of pure β-NiOOH: different chemistries leading to similar overpotentials, J. Am. Chem. Soc. 142 (7) (2020) 3600–3612.
[33] A.J. Tkalych, H.L. Zhuang, E.A. Carter, A density functional+U assessment of oxygen evolution reaction mechanisms on β-NiOOH, ACS Catal 7 (8) (2017) 5329–5339.
[34] A. Govind Rajan, E.A. Carter, Discovering competing electrocatalytic mechanisms and their overpotentials: automated enumeration of oxygen evolution pathways, J. Phys. Chem. C 124 (45) (2020) 24883–24898.
[35] Y.-F. Li, J.-L. Li, Z.-P. Liu, Structure and catalysis of NiOOH: recent advances on atomic simulation, J. Phys. Chem. C 125 (49) (2021) 27033–27045.
[36] Y.-F. Li, A. Selloni, Mosaic texture and double c-axis periodicity of β-NiOOH: insights from first-principles and genetic algorithm calculations, J. Phys. Chem. Lett. 5 (22) (2014) 3981–3985.
[37] A.J. Tkalych, J.M.P. Martirez, E.A. Carter, Effect of transition-metal-ion dopants on the oxygen evolution reaction on NiOOH (0001), Phys. Chem. Chem. Phys. 20 (29) (2018) 19525–19531.
[38] A.G. Rajan, J.M.P. Martirez, E.A. Carter, Strongly facet-dependent activity of iron-doped β-nickel oxyhydroxide for the oxygen evolution reaction, Phys. Chem. Chem. Phys. 26 (20) (2024) 14721–14733.
[39] Y. Zhou, N. López, The role of Fe species on NiOOH in oxygen evolution reactions, ACS Catal 10 (11) (2020) 6254–6261.
[40] J.M.P. Martirez, E.A. Carter, Effects of the aqueous environment on the stability and chemistry of β-NiOOH surfaces, Chem. Mater. 30 (15) (2018) 5205–5219.
[41] M.S. Kim, K.B. Kim, A study on the phase transformation of electrochemically precipitated nickel hydroxides using an electrochemical quartz crystal microbalance, J. Electrochem. Soc. 145 (2) (1998) 507.
[42] A. Šurca, B. Orel, B. Pihlar, P. Bukovec, Optical, spectroelectrochemical and structural properties of sol-gel derived Ni-oxide electrochromic film, J. Electroanal. Chem. 408 (1–2) (1996) 83–100.
[43] S. Grimme, J. Antony, S. Ehrlich, H. Krieg, A consistent and accurate ab initio parametrization of density functional dispersion correction (DFT-D) for the 94 elements H-Pu, J. Chem. Phys. 132 (15) (2010) 154104.
[44] S. Grimme, S. Ehrlich, L. Goerigk, Effect of the damping function in dispersion corrected density functional theory, J. Comput. Chem. 32 (7) (2011) 1456–1465.
[45] A.V. Krukau, O.A. Vydrov, A.F. Izmaylov, G.E. Scuseria, Influence of the exchange screening parameter on the performance of screened hybrid functionals, J. Chem. Phys. 125 (22) (2006) 224106.
[46] R. Dovesi, A. Erba, R. Orlando, C.M. Zicovich-Wilson, B. Civalleri, L. Maschio, M. Rérat, S. Casassa, J. Baima, S. Salustro, Quantum-mechanical condensed matter simulations with CRYSTAL, Wiley Interdiscip. Rev.: Comput. Mol. Sci. 8 (4) (2018) e1360.
[47] J.P. Perdew, K. Burke, M. Ernzerhof, Generalized gradient approximation made simple, Phys. Rev. Lett. 77 (18) (1996) 3865.
[48] M. Cococcioni, S. De Gironcoli, Linear response approach to the calculation of the effective interaction parameters in the LDA+U method, Phys. Rev. B-Condens. Matter Mater. Phys. 71 (3) (2005) 035105.
[49] G. Kresse, J. Hafner, Ab initio molecular dynamics for liquid metals, Phys. Rev. B 47 (1) (1993) 558.
[50] G. Kresse, J. Hafner, Ab initio molecular-dynamics simulation of the liquid-metal–amorphous-semiconductor transition in germanium, Phys. Rev. B 49 (20) (1994) 14251.
[51] G. Kresse, J. Furthmüller, Efficiency of ab-initio total energy calculations for metals and semiconductors using a plane-wave basis set, Comput. Mater. Sci. 6 (1) (1996) 15–50.
[52] G. Kresse, J. Furthmüller, Efficient iterative schemes for ab initio total-energy calculations using a plane-wave basis set, Phys. Rev. B 54 (16) (1996) 11169.
[53] P.E. Blöchl, Projector augmented-wave method, Phys. Rev. B 50 (24) (1994) 17953.
[54] G. Kresse, D. Joubert, From ultrasoft pseudopotentials to the projector augmented-wave method, Phys. Rev. B 59 (3) (1999) 1758.
[55] J.C. Conesa, Electronic structure of the (undoped and Fe-doped) NiOOH O_2 evolution electrocatalyst, J. Phys. Chem. C 120 (34) (2016) 18999–19010.
[56] X. Wang, X. Liu, C.-J. Tong, X. Yuan, W. Dong, T. Lin, L.-M. Liu, F. Huang, An electron injection promoted highly efficient electrocatalyst of $FeNi_3$@GR@Fe-NiOOH for oxygen evolution and rechargeable metal–air batteries, J. Mater. Chem. A 4 (20) (2016) 7762–7771.
[57] M. Kumar, S. Piccinin, V. Srinivasan, Direct and indirect role of Fe doping in NiOOH monolayer for water oxidation catalysis, ChemPhysChem 23 (14) (2022) e202200085.
[58] W. Chen, L. Xu, X. Zhu, Y.C. Huang, W. Zhou, D. Wang, Y. Zhou, S. Du, Q. Li, C. Xie, Unveiling the electrooxidation of urea: intramolecular coupling of the N−N bond, Angew. Chem. Int. Ed. 60 (13) (2021) 7297–7307.
[59] T.E. Jones, D. Teschner, S. Piccinin, Toward realistic models of the electrocatalytic oxygen evolution reaction, Chem. Rev. 124 (15) (2024) 9136–9223.
[60] H. Xiao, H. Shin, W.A. Goddard III, Synergy between Fe and Ni in the optimal performance of (Ni, Fe)OOH catalysts for the oxygen evolution reaction, Proc. Natl Acad. Sci. USA 115 (23) (2018) 5872–5877.
[61] P. Axmann, O. Glemser, Nickel hydroxide as a matrix for unusual valencies: the electrochemical behaviour of metal (III)-ion-substituted nickel hydroxides of the pyroaurite type, J. Alloys Compd. 246 (1–2) (1997) 232–241.
[62] J.Y. Chen, L. Dang, H. Liang, W. Bi, J.B. Gerken, S. Jin, E.E. Alp, S.S. Stahl, Operando analysis of NiFe and Fe oxyhydroxide electrocatalysts for water oxidation: detection of Fe^{4+} by Mossbauer spectroscopy, J. Am. Chem. Soc. 137 (48) (2015) 15090–15093.
[63] A.J. Tkalych, J.M.P. Martirez, E.A. Carter, Thermodynamic evaluation of trace-amount transition-metal-ion doping in NiOOH films, J. Electrochem. Soc. 165 (11) (2018) F907.

[64] R. Dronskowski, P.E. Blöchl, Crystal orbital Hamilton populations (COHP): energy-resolved visualization of chemical bonding in solids based on density-functional calculations, J. Phys. Chem. 97 (33) (1993) 8617–8624.
[65] V.L. Deringer, A.L. Tchougréeff, R. Dronskowski, Crystal orbital Hamilton population (COHP) analysis as projected from plane-wave basis sets, J. Phys. Chem. A 115 (21) (2011) 5461–5466.
[66] S. Maintz, V.L. Deringer, A.L. Tchougréeff, R. Dronskowski, Analytic projection from plane-wave and PAW wavefunctions and application to chemical-bonding analysis in solids, J. Comput. Chem. 34 (29) (2013) 2557–2567.
[67] S. Maintz, V.L. Deringer, A.L. Tchougréeff, R. Dronskowski, LOBSTER: a tool to extract chemical bonding from plane-wave based DFT, J. Comput. Chem. 37 (2016) 1030.
[68] R. Nelson, C. Ertural, J. George, V.L. Deringer, G. Hautier, R. Dronskowski, LOBSTER: local orbital projections, atomic charges, and chemical-bonding analysis from projector-augmented-wave-based density-functional theory, J. Comput. Chem. 41 (21) (2020) 1931–1940.
[69] P.C. Müller, C. Ertural, J. Hempelmann, R. Dronskowski, Crystal orbital bond index: covalent bond orders in solids, J. Phys. Chem. C 125 (14) (2021) 7959–7970.
[70] M. Pauls, D. Schnieders, R. Dronskowski, Embedded localized molecular-orbital representations for periodic wave functions, J. Phys. Chem. A 127 (31) (2023) 6541–6551.
[71] G.A. Landrum, R. Dronskowski, The orbital origins of magnetism: from atoms to molecules to ferromagnetic alloys, Angew. Chem. Int. Ed. 39 (9) (2000) 1560–1585.